

# GRB 221009A: revealing a hidden afterglow during the prompt emission phase with Fermi-GBM observations

HAI-MING ZHANG,<sup>1,2</sup> YI-YUN HUANG,<sup>1,2</sup> RUO-YU LIU,<sup>1,2</sup> AND XIANG-YU WANG<sup>1,2</sup>

<sup>1</sup>*School of Astronomy and Space Science, Nanjing University, Nanjing 210023, China, hmzhang@nju.edu.cn, ryliu@nju.edu.cn, xywang@nju.edu.cn*

<sup>2</sup>*Key laboratory of Modern Astronomy and Astrophysics (Nanjing University), Ministry of Education, Nanjing 210023, China*

(Received 2023 July 24; Revised 2023 September 17; Accepted 2023 September 22)

Submitted to ApJ Letters

## ABSTRACT

Recently, LHAASO reported the detection of brightest-of-all-time GRB 221009A, revealing the early onset of a TeV afterglow. We analyze the spectral evolution of the X-ray/ $\gamma$ -ray emission of GRB 221009A measured by Fermi Gamma-Ray Burst Monitor (GBM) during the dips of two prompt emission pulses (i.e., intervals  $T_0 + [300 - 328]$  s and  $T_0 + [338 - 378]$  s, where  $T_0$  is the GBM trigger time). We find that the spectra at the dips transit from the Band function to a power-law function, indicating a transition from the prompt emission to the afterglow. After  $\sim T_0 + 660$  s, the spectrum is well described by a power-law function and the afterglow becomes dominant. Remarkably, the underlying afterglow emission at the dips smoothly connect with the afterglow after  $\sim T_0 + 660$  s. The entire afterglow emission measured by GBM can be fitted by a power-law function  $F \sim t^{-0.95 \pm 0.05}$ , where  $t$  is the time since the first main pulse at  $T^* = T_0 + 226$  s, consistent with the TeV afterglow decay measured by LHAASO. The start time of this power-law decay indicates that the afterglow peak of GRB 221009A should be earlier than  $T_0 + 300$  s. We also test the possible presence of a jet break in the early afterglow light curve, finding that both the jet break model and single power-law decay model are consistent with the GBM data. The two models can not be distinguished with the GBM data alone because the inferred jet break time is quite close to the end of GBM observations.

*Keywords:* Gamma-ray bursts (629) — High energy astrophysics (739)

## 1. INTRODUCTION

On 9 October 2022, at 13:16:59.99 universal time (UT) (hereafter  $T_0$ ), the Gamma-ray Burst Monitor (GBM) on the Fermi spacecraft triggered and located the burst GRB 221009A (Veres et al. 2022). It is also detected by other gamma-ray detectors, such as the Fermi Large Area Telescope (Fermi/LAT; Pilleri et al. 2022), Konus-Wind (Frederiks et al. 2022, 2023), INTEGRAL (Rodi & Ubertini 2023), Swift-BAT (Krimm et al. 2022), GECAM-C (An et al. 2023; Yang et al. 2023) and LHAASO (LHAASO Collaboration 2023). The exceptionally large fluence of this event saturated almost all gamma-ray detectors during the main burst. The event fluence of GRB 221009A was measured to be  $0.2 \text{ erg cm}^{-2}$  in the energy range of 10 to 1000 keV (Frederiks et al. 2023; An et al. 2023; Lesage et al. 2023), much higher than any previously detected GRB.

LHAASO observed GRB 221009A at the epochs covering both the prompt emission phase and the early afterglow in the TeV band, revealing the onset of afterglow emission in the TeV band as early as  $T_0 + 230$  s and a peak at  $\sim T_0 + 244$  s (LHAASO Collaboration 2023). However, there is no evidence of afterglow emission at such early time at other wavelengths. In the optical to X-rays, the observations start too late (thousands of seconds after the GBM trigger), so they missed the early afterglow. In the hard X-ray to MeV  $\gamma$ -ray energies, as measured by GBM, the prompt emission is so bright that the afterglow emission is likely to be hidden by the prompt emission. The GBM observations show that the last discernible pulse peaking around  $T_0 + 575$  s is followed by a long, smooth decay period (Lesage et al. 2023). Lesage et al. (2023) suggest that this smooth decay is consistent with an afterglow origin. They obtain constraints for the peak of the afterglow at  $\sim T_0 + 600$  s

by fitting the 10 keV extrapolated light curve with two Norris et al. (2005) pulse models for the prompt emission and a broken power-law model (BPL) for the afterglow emission. They tentatively identify this time as the peak of onset of the solely afterglow emission. Additionally, Lesage et al. (2023) obtain different constraints for the peak of the afterglow by extrapolating the smooth emission of the time interval  $T_0 + 597 - T_0 + 1467$  s back in time. Requiring that the extrapolated afterglow flux does not exceed the prompt emission flux, they place a limit of  $t_{\text{peak}} \gtrsim 280$  s assuming the ISM medium for the afterglow emission. As noted in Lesage et al. (2023), all afterglow peak times mentioned above depend on the prompt emission pulse model and the BPL functional fits to the 10 keV extrapolated light curve and therefore are model-dependent.

The apparent discrepancy between the onset time measured from the TeV afterglow and that inferred from the GBM analysis could be due to that the afterglow onset time in the GBM energy range is earlier, but it is hidden by the bright prompt emission (as also argued in Lesage et al. (2023)). Indeed, in GRB 190114C, the afterglow emission is found to overlap with the highly variable prompt emission (Ravasio et al. 2019). Motivated by this, we attempt to search for the afterglow emission at the dips of the GBM emission, where the prompt emission is at the lowest level. We analyze the spectral evolution of the emission of GRB 221009A during two intervals containing the dips (i.e., intervals  $T_0 + [300 - 328]$  s and  $T_0 + [348 - 378]$  s). We also analyze the spectral evolution of the emission after the last pulse peaking around  $T_0 + 575$  s. The data analysis and spectral results will be presented in §2. We find evidence of the transition from the prompt emission to afterglow at the two dips as well as during the period after the last pulse. Combining the afterglow data at the two dips with the late-time afterglow (after  $T_0 + 660$  s), we construct a light curve of the afterglow, which is presented in §3. In this section, we also discuss the modeling and implication of this afterglow component. Finally, we give a summary in §4.

## 2. FERMI-GBM DATA ANALYSIS

Fermi-GBM is composed of twelve sodium iodide (NaI) detectors and two bismuth germanate (BGO) detectors (Meegan et al. 2009). The NaI detectors are sensitive to photons in the energy range from 8 keV to 900 keV, and the BGO detectors are sensitive in 200 keV-40 MeV. GRB 221009A was detected by Fermi-GBM beginning at the trigger time ( $T_0$ ) and lasting until  $T_0 + 1467$  s when it was occulted by the Earth. In this work, we select two NaI detectors (NaI 4 and NaI

8) and one BGO detector (BGO 1) for performing the data analysis, due to that they all have a smaller viewing angle, and the two NaI detectors stay within  $60^\circ$  until  $T_0 + 1467$  s. We retrieved data files from the HEASARC online archive<sup>1</sup> and the corresponding latest updated response matrix files (rsp2) from Lesage et al. (2023). Considering that the spectra analysis of NaI data show deviations between the model and the data below 20 keV<sup>2</sup> (Lesage et al. 2023) and the presence of the Iodine K-edge at 33.17 keV (Bissaldi et al. 2009), we omit the NaI data below 40 keV in our analysis. Following Lesage et al. (2023), we also omit the BGO data below 400 keV in our analysis, due to that the low energy incident photons that are affected by LAT are not adequately modeled in the detector response. Ravasio et al. (2023) reported that a highly significant narrow emission feature around 10 MeV was found in  $T_0 + [280 - 320]$  s, therefore, we ignore the BGO data greater than 8000 keV in order to avoid its possible contamination in our analysis.

The GBM light curve, as shown in panels (a) of Figure 1, 2 and 3, are derived from CSPEC type data<sup>3</sup> of NaI 4, NaI 8 and BGO 1 in the energy range 40–8,000 keV. To model the background, we perform a standard polynomial fitting technique to the light curve over time intervals before and after emission episode. In this work, we select the same background time intervals as that shown in Figure 3 of Lesage et al. (2023), during which a fourth order polynomial fit matches the orbital background estimate the best.

We extract the spectra for this burst with the public Fermi-GBM Data Tools Python software package (GDT; (Goldstein et al. 2022)). We exclude the bad time intervals (BTIs, i.e.,  $T_0 + [219 - 277]$  s (Liu et al. 2023; Lesage et al. 2023) and  $T_0 + [508 - 514]$  s (Lesage et al. 2023)). We start the analysis at  $T_0 + 278$  s to avoid the impact of pile-up, and take 10 s width as a bin until  $T_0 + 508$  s. To assess the spectral evolution after the BTI (i.e. after  $T_0 + 514$  s), we extracted a sequence of 50 s or 100 s width bins until  $T_0 + 1467$  s when it was occulted by the Earth.

We pay special attention to three time intervals of the GBM observations during which the flux drops to a dip: I)  $T_0 + [278 - 328]$  s, II)  $T_0 + [328 - 378]$  s and III)  $T_0 + [514 - 1467]$  s (see the left panels of Figures 1, 2 and 3, where the count rate light curves around these time intervals are shown.). We divide each interval into sev-

<sup>1</sup> <https://heasarc.gsfc.nasa.gov/FTP/fermi/data/gbm/daily/>

<sup>2</sup> In this work, we find that the NaI data also show deviations between the model and the data below 40 keV at  $> 600$  s.

<sup>3</sup> <https://fermi.gsfc.nasa.gov/ssc/data/access/gbm/>

eral time slices for performing spectral analysis, denoted with vertical dashed lines in the left panels of Figures 1, 2 and 3. Throughout our spectral analyses, we test three spectral models, including a Band function (Band; Band et al. (1993)), a power-law (PL), and combinations of them (Band+PL). The results of the spectral analysis of three selected time intervals are reported in Table 1.

To determine the best spectral model for the GBM data of GRB 221009A, we employ Bayesian information criterion (BIC; Schwarz (1978)) to compare different models. The BIC is defined as  $BIC = \chi^2 + k \ln N$ , where  $\chi^2$  is the PGstat statistic,  $k$  and  $N$  are the number of free parameters of the model and the number of data points, respectively. The details of PGstat statistic for the PL, Band and PL+Band models of all time intervals are shown in Table 3 in the Appendix. For interval I ( $T_0 + [278 - 328]$  s), as shown in Table 1, we find that the spectra are best described by the Band function for slices of A and B with high  $\Delta_{BIC}$  values compared with PL function or Band+PL models<sup>4</sup>. For slice C ( $T_0 + [300 - 308]$  s), we find that the combinations of a Band function and a PL provides the best fit with a difference of BIC between the Band function and Band+PL function being  $\Delta_{BIC} = 8.70$ . Later on (i.e., during slices D and E), the spectra are best fitted by PL. This indicates that as the Band component decreases the PL component emerges. Since the prompt emission is usually characterized by a Band function while the afterglow is characterized by a PL, we may see a transition from the prompt emission to the underlying afterglow during this time interval. Our result is consistent with the spectral fitting result of Lesage et al. (2023), in which the authors find that the Band+PL function (with PL index =  $-1.916 \pm 0.009$ ) best fits the data during  $T_0 + [277.894 - 323.975]$  s.

For interval II ( $T_0 + [328 - 378]$  s), we find that that the spectra are best described by the combinations of a Band function and a PL for slices of A and B. For slices C to E, the spectra are best fitted by a PL (see Table 3 in the Appendix). This indicates that the prompt emission component drops and the underlying afterglow component emerges at the dip.

For interval III ( $T_0 + [514 - 1467]$  s), we find that the spectra are best described by the Band function for slices

of A and B. For slices C, we find that the combinations of a Band function and a PL provides the best fit. After this, the spectra in all slices are best fitted by a PL (see Table 3 in the Appendix). Coincidentally, the light curve after slice B shows a remarkably smooth decay in time. Both the spectral and temporal characteristics point to a transition from the prompt emission to the afterglow. The smooth decay after the last pulse has been noticed in the work of Lesage et al. (2023), which also attributed the long, smooth decay period after the final pulse to the afterglow emission. The light curve observed by *INTEGRAL*/IBIS in 200–2600 keV also shows that the afterglow emission begins to dominate at  $\sim T_0 + 630$  s (Rodi & Ubertini 2023).

### 3. AFTERGLOW LIGHT CURVE

We extract the flux of the PL component in the energy range of 50–100 keV and 200–400 keV from the spectral analysis in all slices and plot them in Figure 4 (see the black data points). Adopting the reference time of the afterglow light curve at  $T^* = T_0 + 226$  s (LHAASO Collaboration 2023), we find that these flux points form a remarkable power-law decay in time (see the left panel of Figure 4). The PL fit ( $F \propto t^{\alpha_{pl}}$ ) results in slopes of  $\alpha_{pl} = -0.94 \pm 0.02$  and  $-0.95 \pm 0.05$  for 50–100 keV and 200–400 keV, respectively. This result strongly supports that the PL components in the spectral analysis originate from the afterglow emission. As the first data point of this PL afterglow is at  $T_0 + 300$  s, the peak of afterglow emission of GRB 221009A should be before  $T_0 + 300$  s.

Early TeV observations of GRB 221009A reveals a light curve steepening at  $T_b = T^* + 670^{+230}_{-110}$  s, which is interpreted as a jet break (LHAASO Collaboration 2023). The combined Insight-HXMT and GECAM-C observations of the hard X-ray emission suggests a break in the light curve between  $T^* + 650$  s and  $T^* + 1100$  s (most likely at  $T^* + \sim 950$  s), consistent with the LHAASO result (An et al. 2023). Motivated by this, we study whether a break in the afterglow light curve can be revealed from the GBM data.

First, we compare a broken power-law model having two free slopes with a single power-law model in fitting the light curve of the afterglow emission in 50–100 keV. The best-fitting result gives a slope of  $\alpha_1 = -0.93 \pm 0.02$  before the break and a slope of  $\alpha_2 = -1.82^{+0.42}_{-0.31}$  after the break and a break time of  $t_b = T^* + 1032.41^{+98.55}_{-129.66}$  s. Compared with the single power-law model, the broken power-law model has  $\Delta_{BIC} = 4.64$  ( $\Delta_{BIC}$  is defined as  $BIC_2 - BIC_1$ , where  $BIC_1$  and  $BIC_2$  are the BIC values for the power-law model and broken power-law model,

<sup>4</sup> As suggested by Nunes et al. (2017), the strength of the evidence against the model with the higher BIC value can be summarized as follows. (1) If  $0 < \Delta_{BIC} < 2$ , there is no evidence against the higher BIC model; (2) if  $2 < \Delta_{BIC} < 6$ , positive evidence against the higher BIC model is given; (3) if  $6 < \Delta_{BIC} < 10$ , strong evidence against the higher BIC model is given; (4) if  $\Delta_{BIC} > 10$ , a very strong evidence against the higher BIC model is given.

respectively), indicating that there is no strong evidence against the broken power-law model.

Then, we consider a scenario in which the slopes before and after the break are constrained by the jet break physics (Rhoads 1999; Sari et al. 1999). We consider two possible cases: A) one is that the jet break is due to the edge effect and the light curve steepens by a power of  $\Delta\alpha = 3/4$  (i.e.,  $\alpha_2 = \alpha_1 - 3/4$ ) for a constant-density medium; B) the other is that the sideways expansion effect of the jet is significant so that the post-break decay is  $t^{-p}$  with  $p \simeq 2$  (here we set  $\alpha_2 = -2$ ). In case A, the best-fitting result gives a slope of  $\alpha_1 = -0.92 \pm 0.03$  before the break and a break time at  $t_b = T^* + 1004.75^{+109.29}_{-116.11}$  s. Compared with the single power-law model, the broken power-law model has  $\Delta\text{BIC} = 1.63$ . In case B, the best-fitting result shows that  $\alpha_1 = -0.93 \pm 0.02$ ,  $t_b = T^* + 1055.15^{+81.80}_{-83.42}$  s and  $\Delta\text{BIC} = 1.71$ . We also apply the same analysis to the light curves of the afterglow emission in 200–400 keV. The slopes and break times are all consistent with the case for the 50–100 keV emission within the uncertainty. The fitting results are plotted in the right panel of Figure 4 and summarized in Table 2. The BIC values indicate that the jet break model and the single power-law model fit the data almost equally well. This indicates that a jet break can neither be ruled out nor be favored using the GBM data alone. Nevertheless, the slopes and break time in the jet break model are consistent with those found in the LHAASO data within the  $1\sigma$  uncertainty. The fact that the two models can not be distinguished is understandable since the inferred break time is quite close to the last few points of the GBM data.

We can constrain the lower limit of the jet break time through a chi-squared test (following the  $\chi^2_{N-n}$  distribution with  $N - n = 17$  degrees of freedom, where  $N$  is the number of data points and  $n$  is number of free parameters of the broken power-law model), assuming that the jet break is present. To obtain a useful constraint, we need to fix the slope before the jet break, so we take  $\alpha_1 = -0.93$  following the above analysis. For the jet break scenario in which the light curve steepens by a power of  $\Delta\alpha = 3/4$ , we find that the lower limits (at the 95% confidence level) of the jet break time are 671.2 s for the afterglow in 50–100 keV and 405.7 s for the afterglow in 200–400 keV, respectively. For the jet break scenario in which the post-break decay is  $t^{-2}$ , we find that the lower limits (at the 95% confidence level) of the jet break time are 776.7 s for the afterglow in 50–100 keV and 522.2 s for the afterglow in 200–400 keV, respectively. These lower limits are not in contradiction with the jet break time at TeV energies measured by LHAASO within the uncertainty.

The hard X-ray afterglow emission measured by GBM should be produced by synchrotron emission of relativistic electrons accelerated in the forward shock. In this scenario, as the cooling frequency likely lies below the observed band, the expected photon index is  $dN_\gamma/dE_\gamma \propto E_\gamma^{-(p+2)/2}$ , where  $p$  is the PL index of the electron energy distribution (i.e.,  $dN_e/dE_e \propto E_e^{-p}$ ). The observed photon index in 40–8,000 keV is about  $-2.0$ , implying that  $p \simeq 2.0$ , which is also argued in Lesage et al. (2023). In the synchrotron afterglow model, the expected decay slope is  $F \propto t^{-(2-3p)/4} \simeq t^{-1.0}$  for a spherical shock (Sari et al. 1998). Both the measured pre-break slope in the jet break model and the slope in the single PL decay model are consistent with the expectation (see Table 2).

#### 4. SUMMARY

Through the spectral analysis of the Fermi-GRB data of GRB 221009A, we find clear evidence of afterglow emission during the dips of the prompt emission pulses. The spectra show a transition from the Band function to a PL function during these periods. In the last discernible pulse (around  $T_0 + 660$  s), we also find that the spectrum transits from the Band function to a PL function. During this period, the emerge of the afterglow emission is well consistent with light curve transition from a variable emission to the smooth decaying emission. Remarkably, the afterglow flux at different intervals are smoothly connected in a single power-law, as shown in Figure 4. This suggests that the afterglow peak of GRB 221009A should be  $t_{\text{peak}} \lesssim T_0 + 300$  s.

We also test if there is a jet break in the afterglow emission revealed from the GBM data, motivated by that a jet break is identified in the LHAASO TeV light curve. We find that the jet break model can not be distinguished from the single power-law model using the GBM data alone. This indicates that a jet break can neither be ruled out nor be favored using the GBM data alone. This is understandable since the inferred break time is quite close to the last GBM data. Nevertheless, the slopes and break time in the jet break model are consistent with those found in the LHAASO data. In future, combining the GBM data with other multi-wavelength data, one should be able to reach a conclusive result, which is, however, beyond the scope of the current work.

We thank the anonymous referee for valuable suggestions and thank Stephen Lesage for providing us the latest updated response matrix files and thank Jun Yang for helpful discussion in GBM data analysis. The work is supported by the National Key R&D Program of China under grant No. 2022YFF0711404, the NSFC under grants Nos. 12121003, 12203022 and U2031105, the China Manned Space Project (CMS-CSST-2021-B11) and the Natural Science Foundation of Jiangsu Province grant BK20220757.

## REFERENCES

- An, Z.-H., Antier, S., Bi, X.-Z., et al. 2023, arXiv e-prints, arXiv:2303.01203, doi: [10.48550/arXiv.2303.01203](https://doi.org/10.48550/arXiv.2303.01203)
- Band, D., Matteson, J., Ford, L., et al. 1993, *ApJ*, 413, 281, doi: [10.1086/172995](https://doi.org/10.1086/172995)
- Bissaldi, E., von Kienlin, A., Lichti, G., et al. 2009, *Experimental Astronomy*, 24, 47, doi: [10.1007/s10686-008-9135-4](https://doi.org/10.1007/s10686-008-9135-4)
- Frederiks, D., Lysenko, A., Ridnaia, A., et al. 2022, *GRB Coordinates Network*, 32668, 1
- Frederiks, D., Svinkin, D., Lysenko, A. L., et al. 2023, *ApJL*, 949, L7, doi: [10.3847/2041-8213/acd1eb](https://doi.org/10.3847/2041-8213/acd1eb)
- Goldstein, A., Cleveland, W. H., & Kocevski, D. 2022, *Fermi GBM Data Tools: v1.1.1*.
- Krimm, H. A., Barthelmy, S. D., Dichiara, S., et al. 2022, *GRB Coordinates Network*, 32688, 1
- Lesage, S., Veres, P., Briggs, M. S., et al. 2023, *ApJL*, 952, L42, doi: [10.3847/2041-8213/ace5b4](https://doi.org/10.3847/2041-8213/ace5b4)
- LHAASO Collaboration. 2023, *Science*, 380, 1390, doi: [10.1126/science.adg9328](https://doi.org/10.1126/science.adg9328)
- Liu, R.-Y., Zhang, H.-M., & Wang, X.-Y. 2023, *ApJL*, 943, L2, doi: [10.3847/2041-8213/acaf5e](https://doi.org/10.3847/2041-8213/acaf5e)
- Meegan, C., Lichti, G., Bhat, P. N., et al. 2009, *ApJ*, 702, 791, doi: [10.1088/0004-637X/702/1/791](https://doi.org/10.1088/0004-637X/702/1/791)
- Norris, J. P., Bonnell, J. T., Kazanas, D., et al. 2005, *ApJ*, 627, 324, doi: [10.1086/430294](https://doi.org/10.1086/430294)
- Nunes, R. C., Pan, S., Saridakis, E. N., & Abreu, E. M. C. 2017, *JCAP*, 2017, 005, doi: [10.1088/1475-7516/2017/01/005](https://doi.org/10.1088/1475-7516/2017/01/005)
- Pillera, R., Bissaldi, E., Omodei, N., et al. 2022, *GRB Coordinates Network*, 32658, 1
- Ravasio, M. E., Oganessian, G., Salafia, O. S., et al. 2019, *A&A*, 626, A12, doi: [10.1051/0004-6361/201935214](https://doi.org/10.1051/0004-6361/201935214)
- Ravasio, M. E., Sharan Salafia, O., Oganessian, G., et al. 2023, arXiv e-prints, arXiv:2303.16223, doi: [10.48550/arXiv.2303.16223](https://doi.org/10.48550/arXiv.2303.16223)
- Rhoads, J. E. 1999, *ApJ*, 525, 737, doi: [10.1086/307907](https://doi.org/10.1086/307907)
- Rodi, J., & Ubertini, P. 2023, arXiv e-prints, arXiv:2303.16943, doi: [10.48550/arXiv.2303.16943](https://doi.org/10.48550/arXiv.2303.16943)
- Sari, R., Piran, T., & Halpern, J. P. 1999, *ApJL*, 519, L17, doi: [10.1086/312109](https://doi.org/10.1086/312109)
- Sari, R., Piran, T., & Narayan, R. 1998, *ApJL*, 497, L17, doi: [10.1086/311269](https://doi.org/10.1086/311269)
- Schwarz, G. 1978, *Annals of Statistics*, 6, 461
- Veres, P., Burns, E., Bissaldi, E., et al. 2022, *GRB Coordinates Network*, 32636, 1
- Yang, J., Zhao, X.-H., Yan, Z., et al. 2023, *ApJL*, 947, L11, doi: [10.3847/2041-8213/acc84b](https://doi.org/10.3847/2041-8213/acc84b)

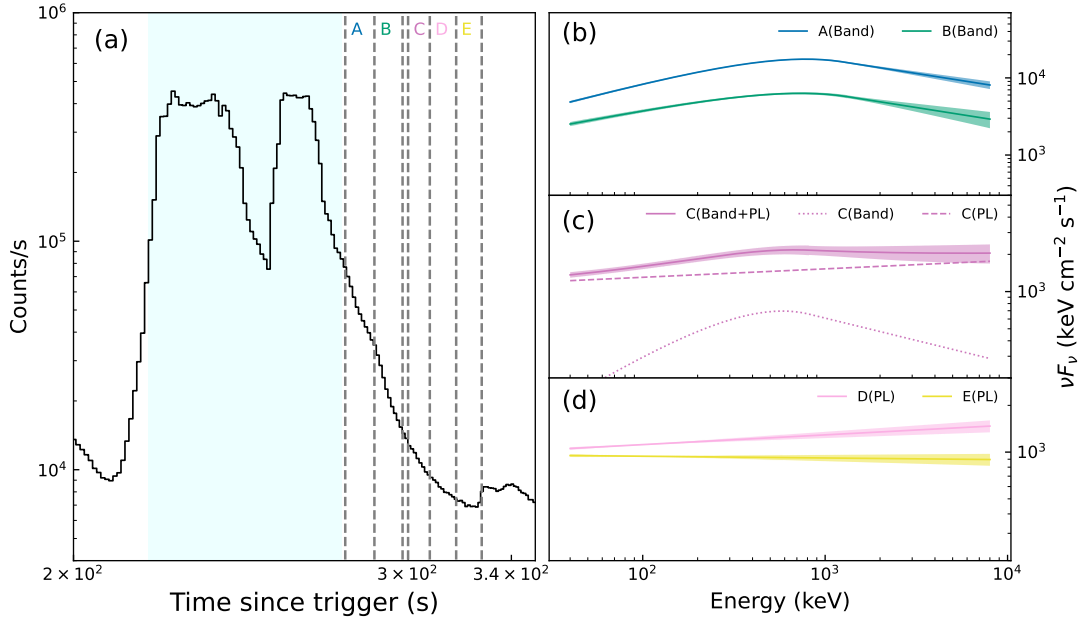


**Figure 1.** (a): The light curve of GRB 221009A in 40–8,000 keV as seen by the NaI 4, NaI 8 and BGO 1 of Fermi-GBM during the interval  $T_0 + [288 - 328]$  s. The light blue vertical shaded region shows the BTI ( $T_0 + [219 - 277]$  s) of Fermi-GBM. The light curve is divided into five time slices (A-E, differentiated by the vertical dashed lines) for the spectral analysis. (b-d): The model spectra in  $\nu F_\nu$  units for all five time slices. The best-fit model for the spectra in slices A and B is the Band function. The best-fit model for the spectrum in slice c is Band+PL function. The best-fit model for the spectra in slices D and E is the PL function .

## APPENDIX

In Figure 5, we show an example of count-rate spectrum during a time interval ( $T_0 + 308 - T_0 + 318$  s) of interest in comparison with the three models. In addition, the values of PGstat statistic and  $\Delta\text{BIC}$  for the PL, Band and PL+Band models of all time intervals are shown in Table 3. Note that, in the time interval  $T_0 + [378 - 388]$  s, the  $\Delta\text{BIC}_{\text{PL}}$  value is only 0.36, implying that there is no evidence against the Band model. Considering the light curve during this interval (as shown in Figure 2) shows a rise, we think that this may be dominated by the prompt emission, and therefore the preferred model is selected to be the Band model.

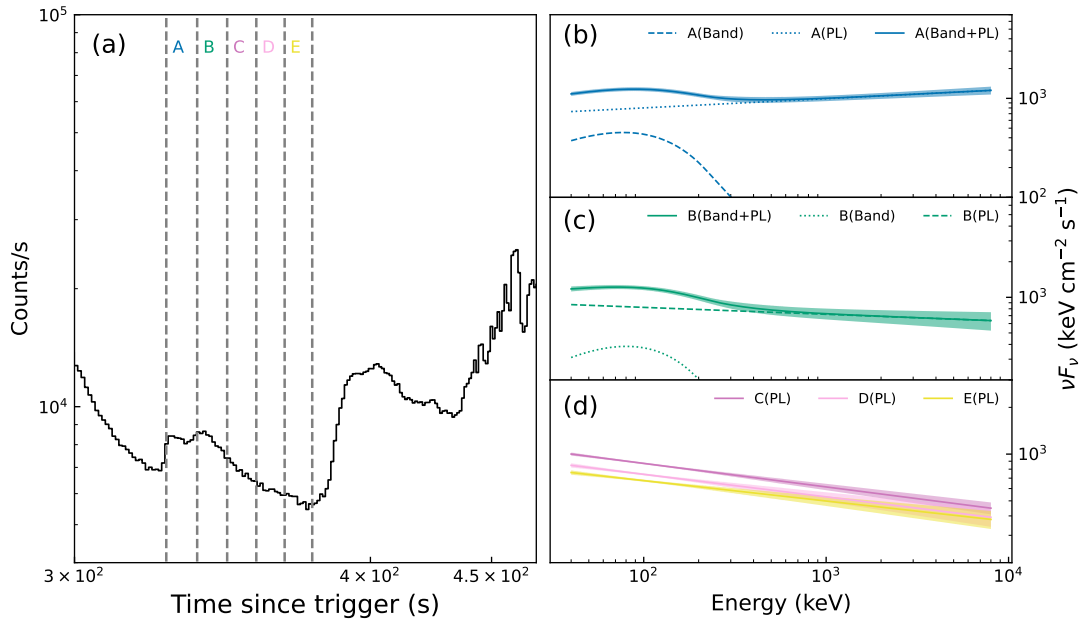


**Figure 2.** Same as Figure 1, but for the time interval  $T_0 + [328 - 378]$  s.

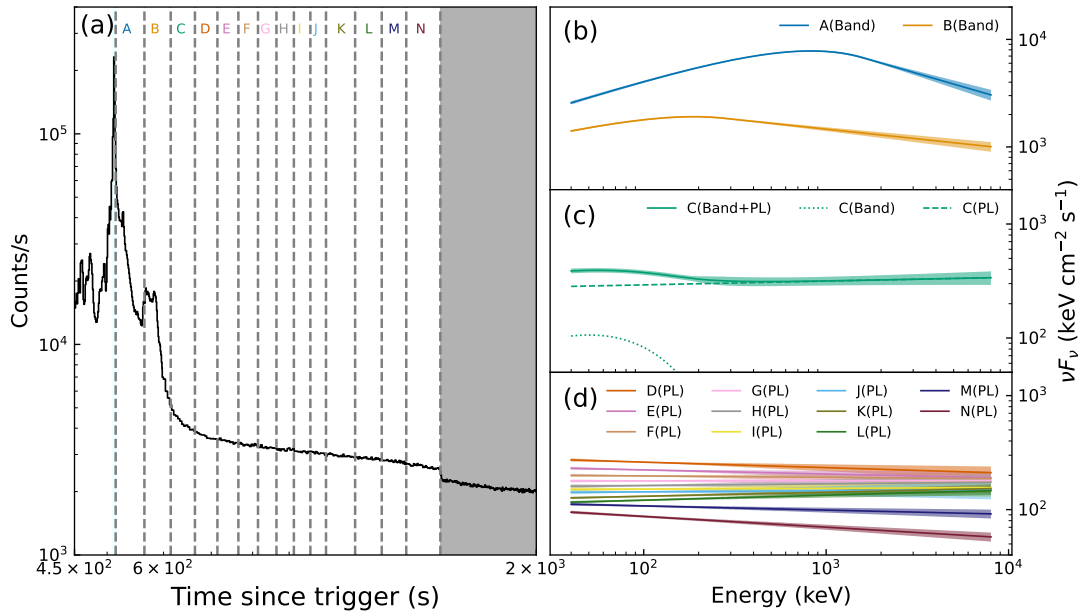


**Figure 3.** Same as Figure 1, but for the time interval  $T_0 + [514 - 1467]$  s.

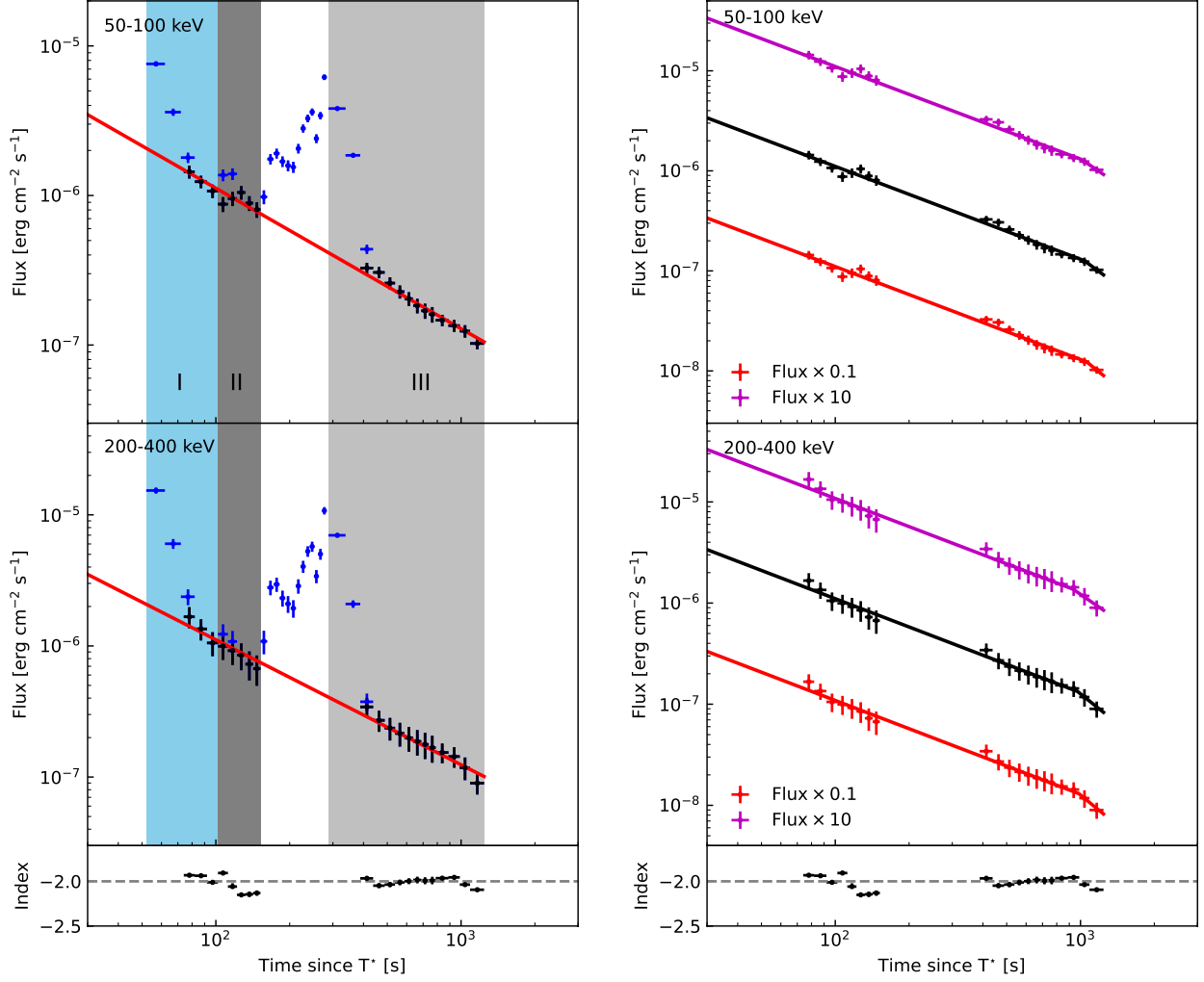


**Figure 4.** Light curve data and modelling of GRB 221009A in 50–100 keV and 200–400 keV. Left panel: The three shaded regions represent the time intervals (I, II and III) that are selected for spectral analysis, as shown in Figure 1, Figure 2 and Figure 3. The blue data points show the flux after fitting the spectra with the best model (Band, PL or Band+PL model), while the black data points show the flux of the PL component extracted from the spectral analysis. The red lines show the fitting of the black data points with a single power-law function, resulting in slopes of  $-0.94 \pm 0.02$  and  $-0.95 \pm 0.05$  for 50–100 keV and 200–400 keV, respectively. Right panel: The afterglow component of GRB 221009A and modeling with the jet break models. The black lines show the fitting with a broken power-law function with free  $\alpha_1$  and  $\alpha_2$ , the magenta lines show the fitting with a broken power-law with free  $\alpha_1$  and  $\alpha_2 = \alpha_1 - 3/4$ , and the red lines show the fitting with a broken power-law with free  $\alpha_1$  and  $\alpha_2 = -2.0$ , respectively. The bottom panels show the evolution of the PL photon index in 40–8,000 keV.



**Table 1.** Spectral fitting results in three time intervals.

Time interval after $T_0$ (s)	$\alpha$	$\beta$	$E_p$ keV	Index	Flux <sub>50–100</sub> <sup>*</sup> erg cm <sup>-2</sup> s <sup>-1</sup>	Flux <sub>200–400</sub> <sup>*</sup> erg cm <sup>-2</sup> s <sup>-1</sup>	PGstat/dof.	Preferred model
Interval I								
A(278 – 288)	$-1.37 \pm 0.01$	$-2.37 \pm 0.06$	$781.31 \pm 16.77$	–	$(7.58 \pm 0.29) \times 10^{-6}$	$(1.53 \pm 0.08) \times 10^{-5}$	632.80/267	Band
B(288 – 298)	$-1.53 \pm 0.02$	$-2.37 \pm 0.13$	$733.73 \pm 34.06$	–	$(3.61 \pm 0.20) \times 10^{-6}$	$(6.02 \pm 0.52) \times 10^{-6}$	444.42/267	Band
(298 – 308)	$-1.77 \pm 0.21$	$-2.11 \pm 0.25$	$1172.97 \pm 316.22$	–	$(1.79 \pm 0.14) \times 10^{-6}$	$(2.37 \pm 0.33) \times 10^{-6}$	296.15/267	Band
C(300 – 308)	$-1.08 \pm 0.10$	$-2.36 \pm 0.30$	$584.16 \pm 69.68$	$-1.93 \pm 0.02$	$(1.44 \pm 0.14) \times 10^{-6}$	$(1.67 \pm 0.31) \times 10^{-6}$	265.39/265	Band+PL
D(308 – 318)	–	–	–	$-1.94 \pm 0.02$	$(1.24 \pm 0.12) \times 10^{-6}$	$(1.35 \pm 0.25) \times 10^{-6}$	330.24/269	PL
E(318 – 328)	–	–	–	$-2.01 \pm 0.02$	$(1.07 \pm 0.11) \times 10^{-6}$	$(1.05 \pm 0.22) \times 10^{-6}$	305.01/269	PL
Interval II								
A(328 – 338)	$-0.91 \pm 0.03$	$-4.01 \pm 0.84$	$77.05^{+2.19}_{-2.15}$	$-1.91 \pm 0.02$	$(8.75 \pm 0.10) \times 10^{-7}$	$(9.95 \pm 2.12) \times 10^{-7}$	280.48/265	Band+PL
B(338 – 348)	$-0.89 \pm 0.03$	$-4.00 \pm 0.66$	$80.31 \pm 2.60$	$-2.06^{+0.04}_{-0.02}$	$(9.54 \pm 1.04) \times 10^{-7}$	$(9.21 \pm 2.04) \times 10^{-7}$	358.25/265	Band+PL
C(348 – 358)	–	–	–	$-2.15 \pm 0.02$	$(1.05 \pm 0.11) \times 10^{-6}$	$(8.49 \pm 1.96) \times 10^{-7}$	338.13/269	PL
D(358 – 368)	–	–	–	$-2.15 \pm 0.03$	$(8.89 \pm 1.00) \times 10^{-7}$	$(7.27 \pm 1.81) \times 10^{-7}$	323.54/269	PL
E(368 – 378)	–	–	–	$-2.13 \pm 0.03$	$(8.04 \pm 0.96) \times 10^{-7}$	$(6.71 \pm 1.74) \times 10^{-7}$	354.94/269	PL
Interval III								
A(514 – 564)	$-1.46 \pm 0.01$	$-2.49^{+0.06}_{-0.07}$	$825.620^{+15.18}_{-14.92}$	–	$(3.81 \pm 0.09) \times 10^{-6}$	$(6.98 \pm 0.25) \times 10^{-6}$	1275.51/267	Band
B(564 – 614)	$-1.60 \pm 0.01$	$-2.18 \pm 0.03$	$187.99^{+3.86}_{-3.75}$	–	$(1.86 \pm 0.06) \times 10^{-6}$	$(2.09 \pm 0.14) \times 10^{-6}$	1058.44/267	Band
C(614 – 664)	$-1.18 \pm 0.02$	$-4.11^{+2.10}_{-0.68}$	$50.28^{+1.85}_{-1.84}$	$-1.97^{+0.03}_{-0.02}$	$(4.37 \pm 0.31) \times 10^{-7}$	$(3.75 \pm 0.58) \times 10^{-7}$	987.09/265	Band+PL
D(664 – 714)	–	–	–	$-2.05 \pm 0.03$	$(3.06 \pm 0.26) \times 10^{-7}$	$(2.71 \pm 0.50) \times 10^{-7}$	1061.35/269	PL
E(714 – 764)	–	–	–	$-2.04 \pm 0.03$	$(2.59 \pm 0.24) \times 10^{-7}$	$(2.36 \pm 0.46) \times 10^{-7}$	1178.75/269	PL
F(764 – 814)	–	–	–	$-2.01 \pm 0.03$	$(2.27 \pm 0.23) \times 10^{-7}$	$(2.15 \pm 0.44) \times 10^{-7}$	1032.81/269	PL
G(814 – 864)	–	–	–	$-2.00 \pm 0.03$	$(2.04 \pm 0.22) \times 10^{-7}$	$(1.99 \pm 0.42) \times 10^{-7}$	1067.46/269	PL
H(864 – 914)	–	–	–	$-1.98 \pm 0.04$	$(1.83 \pm 0.20) \times 10^{-7}$	$(1.87 \pm 0.41) \times 10^{-7}$	908.40/269	PL
I(914 – 964)	–	–	–	$-1.99 \pm 0.04$	$(1.69 \pm 0.20) \times 10^{-7}$	$(1.77 \pm 0.40) \times 10^{-7}$	798.30/269	PL
J(964 – 1014)	–	–	–	$-1.99 \pm 0.04$	$(1.60 \pm 0.19) \times 10^{-7}$	$(1.68 \pm 0.39) \times 10^{-7}$	825.59/269	PL
K(1014 – 1114)	–	–	–	$-1.96 \pm 0.02$	$(1.46 \pm 0.13) \times 10^{-7}$	$(1.54 \pm 0.26) \times 10^{-7}$	1330.05/269	PL
L(1114 – 1214)	–	–	–	$-1.96 \pm 0.02$	$(1.35 \pm 0.12) \times 10^{-7}$	$(1.43 \pm 0.25) \times 10^{-7}$	1042.46/269	PL
M(1214 – 1314)	–	–	–	$-2.04 \pm 0.02$	$(1.24 \pm 0.12) \times 10^{-7}$	$(1.18 \pm 0.23) \times 10^{-7}$	979.62/269	PL
N(1314 – 1467)	–	–	–	$-2.09 \pm 0.02$	$(1.02 \pm 0.09) \times 10^{-7}$	$(8.99 \pm 1.63) \times 10^{-8}$	922.16/269	PL

\* The Flux<sub>50–100</sub> and Flux<sub>200–400</sub> are obtained from Band function for preferred model is Band and PL function for the preferred model is PL (or Band+PL), respectively.**Table 2.** Fitting results of the afterglow light curve in 50-100 keV and 200-400 keV band with jet break models.

Energy band	Power-law			Broken Power-law					
	$\alpha_{pl}$	$\chi^2/dof.$	BIC <sub>1</sub>	$\alpha_1$	$\alpha_2$	$t_b(s)$	$\chi^2/dof.$	BIC <sub>2</sub>	$\Delta BIC$
50-100 keV	$-0.94 \pm 0.02$	12.21/18	18.20	$-0.93 \pm 0.02$	$-1.82^{+0.42}_{-0.31}$	$1032.41^{+98.55}_{-129.66}$	10.86/16	22.84	4.64
				$-0.92 \pm 0.03$	$\alpha_2 = \alpha_1 - 3/4$	$1004.75^{+109.29}_{-116.11}$	10.84/17	19.83	1.63
				$-0.93 \pm 0.02$	$\alpha_2 = -2.0$	$1055.15^{+81.80}_{-83.42}$	10.92/17	19.91	1.71
200-400 keV	$-0.95 \pm 0.05$	4.22/18	10.21	$-0.93 \pm 0.05$	$-1.95^{+1.00}_{-0.75}$	$969.06^{+130.26}_{-188.80}$	2.18/16	14.70	4.49
				$-0.92 \pm 0.05$	$\alpha_2 = \alpha_1 - 3/4$	$927.72^{+154.84}_{-149.15}$	2.83/17	11.82	1.61
				$-0.93 \pm 0.05$	$\alpha_2 = -2.0$	$981.49^{+128.98}_{-121.48}$	2.73/17	11.72	1.51

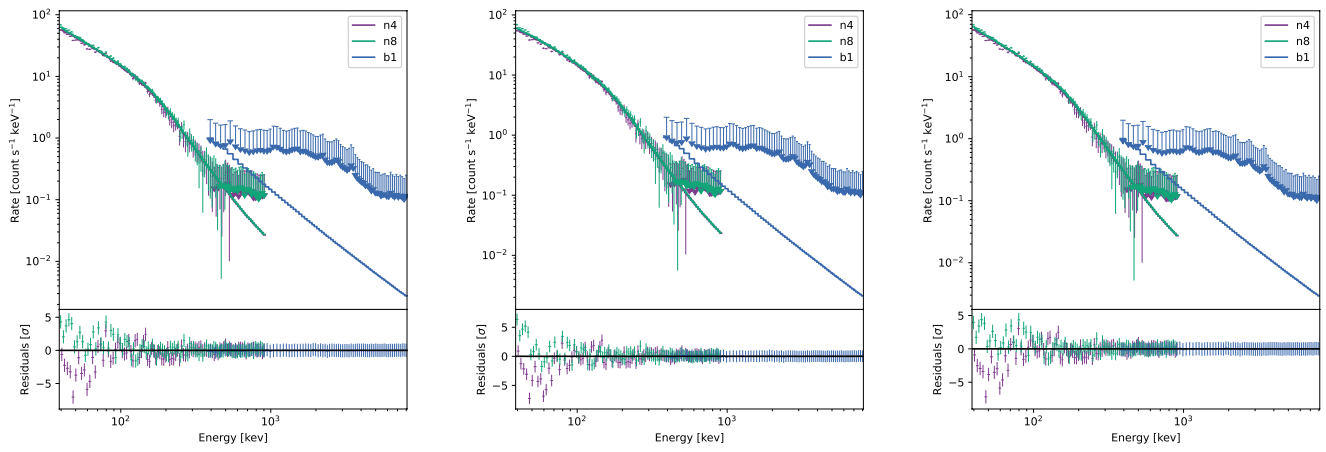


**Figure 5.** An example of the count-rate spectrum (during the interval  $T_0 + 308 - T_0 + 318$  s) in comparison with the PL (left panel), Band (middle panel) and Band+PL (right panel) models, respectively. The corresponding statistics for the fits are shown in Table 3 in Appendix.

**Table 3.** The values of PGstat statistics and  $\Delta\text{BIC}$  for the PL, Band and PL+Band model of all time intervals.

Time interval after $T_0$ (s)	PGstat/dof. PL	PGstat/dof. Band	PGstat/dof. Band+PL	$\Delta\text{BIC}_{\text{PL}}^\dagger$	$\Delta\text{BIC}_{\text{Band}}^\dagger$	$\Delta\text{BIC}_{\text{Band+PL}}^\dagger$	Preferred model
278 – 288	17173.77/269	632.80/267	870.21/265	16529.76	0	248.61	Band
288 – 298	1554.85/269	444.42/267	490.05/265	1099.22	0	56.83	Band
298 – 308	351.74/269	296.15/267	297.74/265	44.38	0	12.79	Band
300 – 308	296.43/269	285.29/267	265.39/265	8.63	8.70	0	Band+PL
308 – 318	330.24/269	362.23/267	329.56/265	0	43.20	21.73	PL
318 – 328	305.01/269	305.08/267	298.35/265	0	11.28	11.75	PL
328 – 338	334.11/269	303.93/267	280.48/265	31.22	12.25	0	Band+PL
338 – 348	440.86/269	398.23/267	358.25/265	60.20	28.78	0	Band+PL
348 – 358	338.13/269	333.50/267	338.13/265	0	6.58	22.41	PL
358 – 368	323.54/269	322.50/267	323.53/265	0	10.17	22.40	PL
368 – 378	354.94/269	356.44/267	346.65/265	0	12.71	14.12	PL
378 – 388	295.40/269	283.83/267	286.85/265	0.36	0	14.22	Band
388 – 398	834.46/269	308.39/267	302.02/265	514.86	0	4.83	Band
398 – 408	936.85/269	335.18/267	355.43/265	590.46	0	31.45	Band
408 – 418	643.77/269	330.05/267	329.81/265	302.51	0	10.96	Band
418 – 428	552.77/269	320.37/267	319.58/265	221.19	0	10.41	Band
428 – 438	518.97/269	322.26/267	320.69/265	185.50	0	9.63	Band
438 – 448	802.55/269	380.78/267	380.44/265	410.56	0	10.86	Band
448 – 458	1110.69/269	337.61/267	338.79/265	761.87	0	12.38	Band
458 – 468	1722.38/269	441.86/267	440.23/265	1269.31	0	9.57	Band
468 – 478	1739.68/269	475.96/267	475.51/265	1252.51	0	10.75	Band
478 – 488	943.27/269	319.04/267	319.20/265	613.02	0	11.36	Band
488 – 498	1351.62/269	333.68/267	340.97/265	1006.73	0	18.49	Band
498 – 508	3674.84/269	481.75/267	534.21/265	3181.88	0	63.66	Band
514 – 564	8754.23/269	1275.51/267	1552.14/265	7467.51	0	287.83	Band
564 – 614	2107.49/269	1058.44/267	1109.73/265	1037.84	0	62.49	Band
614 – 664	1012.37/269	1012.85/267	987.09/265	10.71	14.57	0	Band+PL
664 – 714	1061.35/269	1060.86/267	1057.92/265	0	10.72	18.98	PL
714 – 764	1178.75/269	1698.63/267	1178.68/265	0	531.09	22.34	PL
764 – 814	1032.81/269	1066.33/267	1032.50/265	0	44.73	22.10	PL
814 – 864	1067.46/269	1080.44/267	1067.44/265	0	24.19	22.39	PL
864 – 914	908.40/269	916.15/267	901.63/265	0	18.96	15.64	PL
914 – 964	798.30/269	803.67/267	798.18/265	0	16.58	22.29	PL
964 – 1014	825.59/269	828.18/267	822.71/265	0	13.8	19.53	PL
1014 – 1114	1330.05/269	1330.08/267	1328.73/265	0	11.23	21.09	PL
1114 – 1214	1042.46/269	1048.54/267	1028.10/265	0	17.29	8.05	PL
1214 – 1314	979.62/269	979.79/267	977.70/265	0	11.38	20.49	PL
1314 – 1467	922.16/269	922.26/267	922.08/265	0	11.31	22.33	PL

$\dagger$  The  $\Delta\text{BIC}_{\text{PL}}$ ,  $\Delta\text{BIC}_{\text{Band}}$  and  $\Delta\text{BIC}_{\text{Band+PL}}$  are defined as  $\Delta\text{BIC}_{\text{PL}} = \text{BIC}_{\text{PL}} - \text{BIC}_{\text{Preferred model}}$ ,  $\Delta\text{BIC}_{\text{Band}} = \text{BIC}_{\text{Band}} - \text{BIC}_{\text{Preferred model}}$  and  $\Delta\text{BIC}_{\text{Band+PL}} = \text{BIC}_{\text{Band+PL}} - \text{BIC}_{\text{Preferred model}}$ .